

Mantle instability beneath the Sierra Nevada Mountains in California and Death Valley extension

Laetitia Le Pourhiet^{*}, Michael Gurnis, Jason Saleeby

Division of Geological and Planetary Sciences, California Institute of Technology, Pasadena, CA 91125, USA

Received 25 April 2006; received in revised form 29 August 2006; accepted 30 August 2006

Available online 11 October 2006

Editor: Scott King

Abstract

The Southern Sierra Nevada mountain range rapidly uplifted at ≈ 3.5 Ma simultaneously with a pulse of basaltic volcanism. Xenoliths recovered from volcanics indicate that the range lost a dense crustal root after the Miocene. The vertical motions and removal of the root have been linked to a fast seismic velocity anomaly that extends ≈ 200 km into the mantle but is offset to the west of the range. With visco-elasto-plastic thermo-mechanical numerical models, we have tested the influence of crustal strength on the kinematics of removal and on the amount of associated uplift. We find that delamination of the dense root is the most likely mechanism for gravitational instability to occur. The model satisfies the Plio-Quaternary vertical motions, the shift of the mantle anomaly to the west of the range, and intense Miocene extension to the east. Based on those results, we propose the existence of a dynamic link between the Sierra Nevada mantle instability and Death Valley rifting.

© 2006 Elsevier B.V. All rights reserved.

Keywords: gravitational instability; Sierra Nevada; Death Valley; Cordilleran Arcs dynamic; thermo-mechanical modeling

1. Introduction

Convective removal of continental lithosphere is likely a fundamental process affecting the evolution of Earth's mantle and landscape [1–3]. Although convective instability of the lithosphere has been the subject of considerable conjecture, the putative Plio-Pleistocene removal of a high-density crustal root beneath the Sierra Nevada Mountains in California (USA) allows a link to be made between geodynamic concepts and a broad range of observations at a level not previously achieved

[4–7]. Here we substantially broaden this linkage through thermo-mechanical models that are constrained by seismic, petrologic, structural and geomorphologic observations. Before proceeding to a description of the models and their implications, we briefly present the major geologic constraints and motivations.

2. Geological setting

The Sierra Nevada range and the Great Valley distinguish themselves in the diffuse North America/Pacific plate boundary by their semi-rigid behavior (“block”) and thus may be designed as a microplate [8]. This micro-plate is bounded by the San Andreas Fault on the west and the Eastern Sierra Fault system (ESFS) on the east (Fig. 1). It was formed when the Basin and

^{*} Corresponding author. GPS; Caltech, Mail code 252-21, 1200 E California Blvd, Pasadena, CA 91125, USA. Tel.: +1 626 395 8019; fax : +1 626 564 0715.

E-mail address: laetitia@gps.caltech.edu (L. Le Pourhiet).

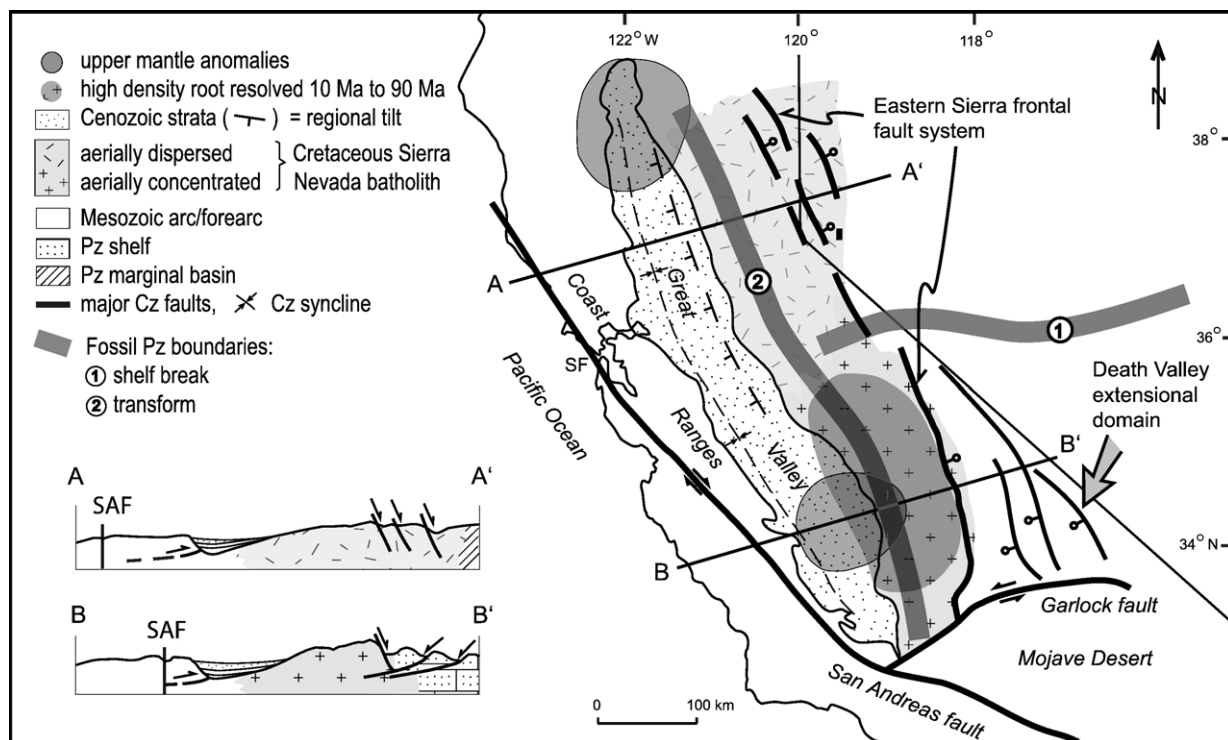


Fig. 1. Geological sketch map and cartoon cross-sections. Cz=Cenozoic; Pz=Paleozoic; SAF=San Andreas Fault; GV=Great Valley; SN=Sierra Nevada; BR=Basin and Range; DV=Death Valley. Paleozoic contacts: 1: shelf break of the passive margin with slope directed to the north-west; 2: transform truncation zone along which Mesozoic subduction arc system nucleated.

Range extension that had been migrating to the west from the middle Miocene, finally localized at the eastern border of the Sierra Nevada batholith. The kinematics of the ESFS is constrained from the stratigraphic expression of fault growth through the Neogene volcanogenic sequences between latitudes 38° and 39° N and from thermochronometric data from basement rocks exhumed along fault scarps at latitudes $\sim 39^{\circ}$ N and $\sim 36.5^{\circ}$ N. Its inception at 10 Ma correlates in time with the inception of left-lateral transfer faulting on the Garlock fault [9–12].

In contrast with the apparent rigidity of the microplate, distinct kinematics occur from north to south within the microplate. The polarity of the major Miocene normal faults of the ESFS switches from east-dipping in the north [10, 13] to west-dipping in the south [14]. Neogene to Recent sedimentation patterns in the Great Valley also change across this N–S transition zone. Progressive offlap of the strata from the west flank of the northern Sierras (Fig. 1 AA') reflects west tilting of the microplate controlled by east-dipping normal faults of the ESFS [10, 13]. In contrast, these strata onlap the southwestern Sierra basement (Fig. 1 BB') as the eastern margin of the Tulare sub-basin of the Great

Valley [15]. This implies tectonic creation of accommodation space, or sediment loading due to a rapid increase in differential elevation between the eastern Sierra and the adjacent western Sierra–Great Valley.

The north–south differences in ESFS fault geometry and Great Valley sedimentation patterns are inherited from batholithic crustal structure which was in turn inherited from major tectonic features of the Paleozoic host rock complex for the batholith. These north–south transitions occur at the latitude of the northern edge (shelf break) of the E–W-trending Paleozoic passive margin which extended into the host for the batholith (Fig. 1). The batholith had localized itself along a late Paleozoic transform system which sharply truncated the passive margin, and along which the Mesozoic active margin subsequently nucleated. Hence, the southern and northern segments of the batholith developed in contrasting source regimes. Crustal thickness and compositional differences between the continental passive margin, and the northern oceanic offshore facies hosts led to a deeper level melting interval for felsic melt production of the batholith in the south. As shown by mantle xenolith studies this in turn led to the accumulation of a substantial residue sequence in the south,

equilibrating in the eclogite facies [5,6]. Based on those assumptions, we hypothesize that the dense crustal root of the southern batholith was a direct result of it having developed within continental lithosphere, and that the northern batholith lacked such an extensive root. Mantle xenolith studies further show that the high-density eclogitic root for the southern batholith, as well as associated mantle wedge peridotites, remained intact at least until 10 Ma (late Miocene).

At 3.5 Ma, the southern Sierra rapidly gained ≈ 600 m in elevation [16]. Simultaneously with the uplift, a pulse of basaltic volcanism originating from decompression partial melting of depleted mantle (asthenosphere) set in. Unlike the Miocene record, the xenoliths from the Plio-Quaternary lavas show no evidence for a deep mafic root and the lavas reflect partial melting at higher temperatures and shallower depths [5]. The simultaneity of uplift and onset of Plio-Quaternary volcanism, as well as the presence of a clearly imaged high seismic velocity anomaly that extends ≈ 200 km in depth beneath the western Sierra and Great Valley [4, 17], strongly suggests that the loss of a dense crustal root triggered the uplift of the southern Sierra.

3. Modeling assumptions

3.1. Forces and modeling approach

Since the crustal ultra-mafic root of the Sierra was likely denser than the mantle, its rapid removal at 3.5 Ma, as a result of a gravitational instability, is the most plausible explanation for its removal. A Rayleigh–Taylor (RT) instability is in general proposed to explain the removal of dense lithospheric roots. This model describes the lithosphere and asthenosphere as a mechanical system with two infinite layers of viscous fluid of contrasting density. Initial perturbation of this unstable equilibrium leads to instability and diapirism.

Assuming a non-linear wet olivine creep law, the RT model predicts that only material between the 1300 °C (asthenosphere) and 800 °C isotherms would be removed [3]. According to xenolith thermo-barometry, the dense garnet pyroxenite body is not located in this range of temperature (apart from its base), and hence, an RT instability will not allow its full removal if viscosity depends on temperature. Nevertheless, assuming that (1) the strain rate is constant throughout the lithosphere regardless of its temperature gradient (thin sheet approximation), (2) the mantle lithosphere (35–195 km depth) possesses a constant density contrast of $\delta\rho = 200 \text{ kg m}^{-3}$ with the underlying asthenosphere, and (3) the initial perturbation has an amplitude of 80 km,

the RT model would predict a 7 Myr time scale for root removal, consistent with values inferred for the Sierra Nevada [18]. However, based on the densities and geometry of the layers, we estimate that this model gives an isostatic uplift of up to 15 km, a factor of ~ 10 larger than inferred geologically while predicting a symmetric anomaly beneath the Sierra, inconsistent with the location and shape of the seismically imaged anomaly.

Consequently, we proceed to investigate gravitational instabilities in the lithosphere without prescribing flow kinematics, using a thermo-mechanical approach that gives substantially different solutions than classical RT models.

We fix the parameters that are well constrained by geology (initial geotherms, geometry of the different crustal terranes, elastic and brittle rheological parameters) and study the effects of varying the least constrained (creep parameters) upon the occurrence and kinematics of resulting gravitational instabilities. Numerical experiments allow us to determine the evolution of strength with time and relate its variation to a range of observable quantities (from seismology to structural geology). Because the rejuvenation of relief of the Sierra occurred over millions to tens of millions years, we need to account for thermo-chemical mantle convection without neglecting the softening from elasto-plasticity at the surface. Consequently, we use a thermo-mechanical code based on the FLAC method [19, 20], which allows modeling realistic topography, visco-elasto-plastic thermo-dependant rheologies and temperature and compositional dependence of density (Appendix A).

Two parameters mainly control the integrated strength of the lithospheric column: the thickness of the thermal boundary layer and the mechanical coupling between the crust and the mantle. We first present our assumptions concerning these parameters before demonstrating their influence on the kinematics of gravitational instability.

3.2. Assumptions regarding the initial geotherm

In the case of the Sierra Nevada, given the current shallow depth of the asthenosphere on the eastern side of the Sierra with an associated low surface heat flux (40 mW m^{-3}), one may conclude that the current geotherm is not in equilibrium and that the current flux at the surface is a remnant of the initial geotherm. Moreover, petrological study of the Sierra's mafic root and mantle Xenoliths have shown that the temperature at 90 km depth did not exceed 900 °C before the removal of the root and rejuvenation of relief. Thus, there are good constraints on the initial geotherm within the upper 90 km of the lithosphere. However, below 90 km, the details of the geotherm remain conjectural.

We hypothesize that the cold geotherm of the surface was caused by the inverse geothermal gradient associated with Farallon plate subduction until 30 Ma [21, 22]. This protects the chemistry of the region sampled by the deep xenoliths by the advection of cold material below the Sierra. By the time subduction resumed, the subducted plate below the Sierra was not older than 10 Myr [22] and even though the temperature was cool, the heat flux was higher than 150 mW m^{-2} at the base of the Sierras [23]. At that time, either a slab gap was filled by the emplacement of asthenosphere immediately below the Sierra root between 20 and 30 Ma, or the thin remnant of Farallon slab (less than 30 km) warmed by conduction or was removed by small-scale convection. In either case, a high temperature gradient existed at 20 Ma at around 90 km depth.

For these reasons, the initial geotherm has been computed independently using a FEM code that solves for Laplace's equation for both stationary and non-stationary cases (Appendix B). In order to account for the stable subduction geotherm prior to 30 Ma, a 1D stationary solution was first computed with surface heat flux (40 mW m^{-2}) and xenolith constrained temperature ($900 \text{ }^\circ\text{C}$ at 90 km) as boundary conditions. Our models are meant to start at around 20 Ma. In order to account for the effect of the thermal destabilization caused by the disruption of subduction and onset of volcanism at 30–20 Ma [22], a transient solution of the heat equation has been computed for the 10 Myr time interval following the disruption of subduction (i.e., from 30 to 20 Ma), using the previous steady state solution as initial condition and setting temperature at $1300 \text{ }^\circ\text{C}$ at the top of the slab and at all the nodes located below 90 km depth in the model. The mantle geotherm was computed explicitly to match an adiabatic gradient from 90 km depth to 396 km ($1420 \text{ }^\circ\text{C}$). The resulting geotherm thus possesses a rather low surface heat flow, and a high temperature gradient at the base of the lithosphere.

3.3. Mechanical coupling of the crust and mantle

Mechanical decoupling between the crust and mantle is known to cause substantial reduction in lithospheric strength by reducing both the elastic thickness of the lithosphere [24] and the effective viscosity of the upper mantle (as the boundary conditions at the top of the convective part of the system becomes a free surface). The level of coupling primarily depends on the chemical nature of the rock and on the Moho temperature. Although we know that the temperature at the Moho is in the range of $300\text{--}400 \text{ }^\circ\text{C}$ and the crust is mainly composed of Quartz down to 35 km in the batholith [25],

ascertaining creep parameters from the literature remains uncertain, especially for crustal material. Published parameters for quartz/granite materials (see review in [26]) lead to substantially different stress–strain rate relationships at the base of the crust (Fig. 2A). One may thus consider that the rheology of the crust is the least constrained model parameter. It is rather difficult to compare those creep laws because they typically depend on three parameters (A , Q , n , Eq. (A5)). Following [27], we chose one set of quartz creep parameters (A_0 , Q_0 , n_0) and introduce a second pre-exponential factor C such that $A=CA_0$ while $Q=Q_0$ and $n=n_0$; thus for a given stress and temperature, $C=\eta_0/\eta$ and can be considered as a viscosity ratio. It allows for varying the strength of the lower crust in a range inferred by different sets of parameters found in the literature (Fig. 2B) without having three parameters changing simultaneously.

To test our hypothesis, we used a simple layered set up featuring a high temperature gradient at the base of a gravitationally unstable layer (Fig. 3A). The model presented on the left of the figure was run without decoupling between the crust and mantle while the

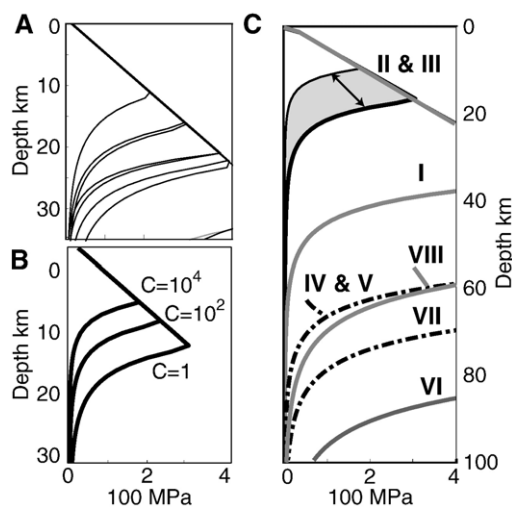


Fig. 2. Strength of the lithosphere. All envelopes are plotted for a strain rate of 10^{-15} s^{-1} and a geotherm corresponding to the steady state deduced from the xenoliths of the Sierra. (A) Black lines represent strength envelopes for the different quartzite set of rheological parameter listed in [26]. The surface located between the strongest and weakest possible envelope according to laboratory measurement uncertainties has been shaded in black with 10% of opacity. Thus, the darkest part of the plot is the place where the error areas of the different set of parameters overlap the most. (B) Plot with the same geothermal gradients and the same strain rate as (A) for the set of rheological parameters used for this study with $C=1$, $C=10^2$ and $C=10^4$. (C) The first 100 km strength envelopes of the different lithologies of the models. Roman numbers correspond to entries of Table 1.

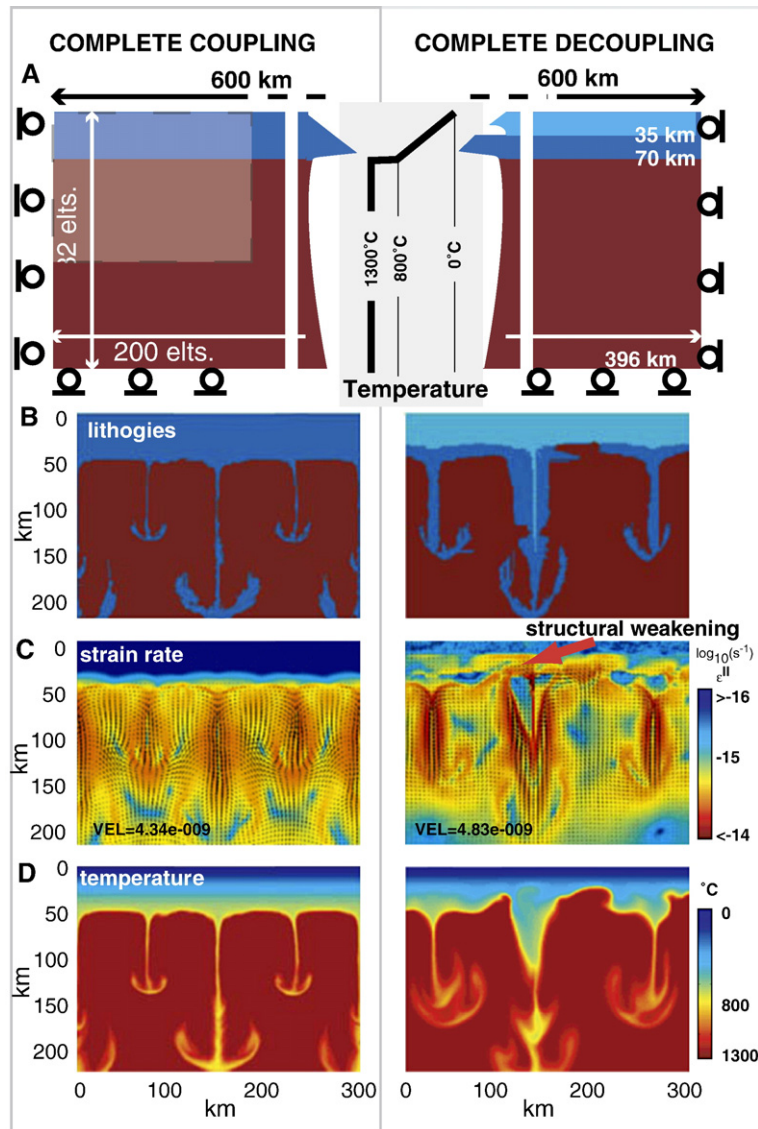


Fig. 3. Impact of mantle/crust coupling on gravitational instabilities: (A) Initial and boundary conditions of the models, associated strength envelopes, the black circles mean free slip boundary conditions; (B–D) results after 7 Myr for symmetry reason only the white shaded area in (A) is represented. (B) The drips are much wider in the case of a decoupled crust and some of the upper crust thickens at the level of the mantle drips. (C) In the decoupled case, the deformation is much more localized in the mantle resulting in a very non-linear behavior of the instabilities. The lower crust is also deforming under the influence of the drips creating local couette flows directed towards the drips. (D) The temperature field reflects the mode of advection, but only the decoupled case models may be detected by regional tomographic arrays.

adjacent model was run using crust decoupled from the mantle. For symmetry reasons, only half of the numerical boxes are displayed, nevertheless the introduction of a secondary length scale in the system has caused loss of symmetry (Fig. 3B). After 7 Myr of evolution, the anomalously dense layer of the coupled model has been slowly eroded by repeated small-scale Rayleigh–Taylor (RT) instabilities while the decoupled model has evolved into large drips of cold and dense material

(Fig. 3B and D). The strain rate (Fig. 3C) shows that in the coupled case, the lithosphere is not affected by the deep processes (as demonstrated by negligible strain rate in the upper 45 km of the model). In the decoupled model, the large drips are relatively rigid and surrounded by localized shear zones both in the lower crust and upper mantle.

As the timing of the removal (7 Myr) is similar to the timing obtained using viscous nonlinear RT models that

allows a pseudo-plastic criterion [28] to reduce the strength of the lithosphere in its upper part [18], we believe that this mechanism could explain the fast removal of the Sierra root. The originality of the approach is that instead of inferring the reduction of the strength to some intra-crystalline localization process observed in the laboratory at scales that are not relevant to the lithosphere, our model inferred that the strength drop is of a structural nature. The non-linearity of the mechanical behavior of the model is associated with localization in the lower crust and relates to specific structural precursors that one may constrain from structural geology. Moreover, this model, unlike the coupled case, predicts drips that are large enough to be resolved by regional seismic arrays. It also predicts deflection of the Moho that are compatible with the “Moho hole” imaged by receiver functions in the southern Sierra [4] (Fig. 3A). Nevertheless, it does not explain the eastern dip of the seismic wave travel time anomaly beneath the Sierra.

3.4. More realistic model set-up

It is necessary to develop more geologically reasonable initial conditions, so that we can compare the model to observations. Initially, the model domain is 600 km by 396 km deep representing E–W vertical sections across the southern Sierra and the Death Valley extensional system. Hereafter, the right and left side of the domain are referred to as east and west, respectively. During the computation, free-slip boundary conditions are applied on all the boundaries except the top boundary, which behaves as a free surface. The normal velocity is set to zero at the east margin and at the base. Extension is applied by fixing the westward horizontal velocity to 5 mm yr^{-1} on the west margin.

The initial geometry and composition of the crust, crustal root and lithosphere (Fig. 4) are based on surface geological observations of differentially exhumed crustal rocks, and mantle xenoliths [29]. The main assumptions are that the crustal root only exists below the batholith and that the batholith and the eastern part of the models have a weaker lower crust than the Great Valley. The second assumption is mainly based on the argument that the Great Valley is a fore arc basin while the batholith and the Death Valley extensional system are of continental affinity in the Southern Sierra.

Model phase densities are taken from gravimetric inversion in the southern Sierra [30], and topography is initially in isostatic equilibrium unless otherwise stated. The mechanical properties of the different phases are detailed in Table 1 and their associated strength envelopes are shown according to the initially cold

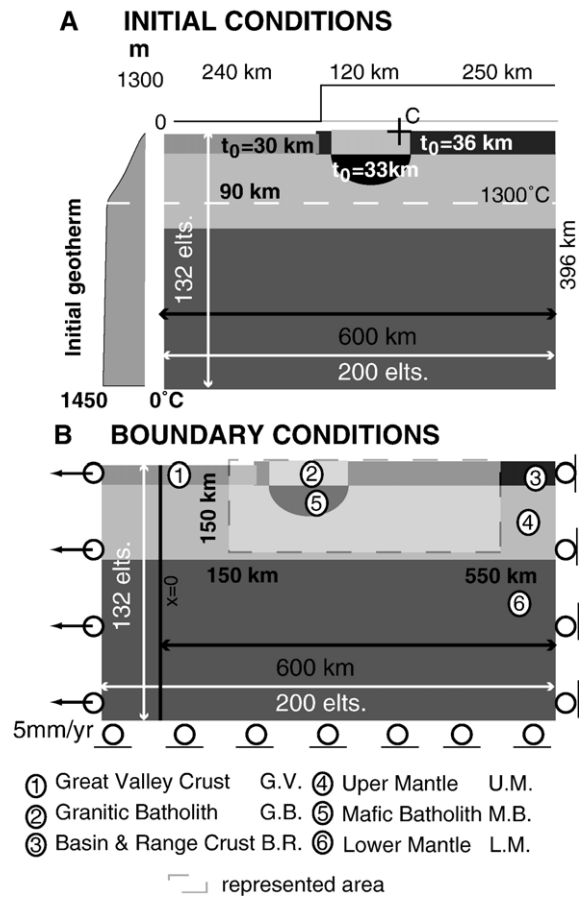


Fig. 4. Initial and boundary conditions for the realistic models. On both plots, the gray scale code highlights the initial distribution of each of the lithological units. elts means mesh elements. (A) Initial conditions. The line at the top outlines the initial topography for the models which account for one. Dashed white line is the 1300 °C isotherm limiting the conductive temperature field from an adiabatic solution. C is the future crest of the Sierra. t_0 refers to the initial thickness of the layers. (B) Black circles indicate free slip boundary conditions. Arrows indicate the applied normal velocity is not null. The top boundary is a free surface (τ and σ_n are both set to zero on the deformable interface).

geotherm (Fig. 4C). The rheological parameters associated with the different lithological units are summarized in Table 2 for each of the presented models.

4. Mechanics of delamination

The evolution of Model A is detailed in Fig. 5. The height of the eastern edge of the batholithic crust (Point C) evolves through time with three main inflections (Fig. 5E) that are representative of major strength transition at lithospheric scales: (1) a period of slow uplift precedes the localization of the strain in the upper crust at 6.3 Myr, (2) a period of accelerating subsidence at the time of lithospheric break-up between 9 and 11 Myr, and (3) rapid uplift

Table 1
Rheological parameters

Phase number	ρ (kg m ⁻³)	n (adim.)	A (MPa ⁻ⁿ)	E (J mol ⁻¹)	λ (Pa)	μ (Pa)	C_0 (Pa)	ϕ (°)	k (Wm ⁻¹ k ⁻¹)
I [40]	2840	3.05	6.30×10^{-2}	2.75×10^5	3×10^{10}	3×10^{10}	2×10^7	30	3.0
II [26]	2700	3	$C \times 6.80 \times 10^{-6}$	1.56×10^5	3×10^{10}	3×10^{10}	2×10^7	30	2.5
III [26]	2810	3	$C \times 6.80 \times 10^{-6}$	1.56×10^5	3×10^{10}	3×10^{10}	2×10^7	30	2.5
IV [41]	3300	3.4	1.9×10^3	4.20×10^5	9×10^{10}	3×10^{10}	2×10^7	30	3.5
V [41]	3410	3.4	1.9×10^3	4.20×10^5	3×10^{10}	3×10^{10}	2×10^7	30	3.5
VI [42]	3300	3.5	2.4×10^5	5.40×10^5	9×10^{10}	3×10^{10}	2×10^7	30	3.5
VII [43]	3410	3.4	1.9×10^3	4.20×10^5	3×10^{10}	3×10^{10}	2×10^7	30	3.5
VIII [44]	2840	4.7	190	4.85×10^5	3×10^{10}	3×10^{10}	2×10^7	30	3.0

λ and μ are Lamé elastic moduli ϕ and C_0 are, respectively, friction angle and Cohesion, ψ the dilatation angle is set to 0°, k and ρ are thermal conductivity and chemical density, thermal expansion α is set 2.5×10^{-5} K⁻¹. n , A and E are viscous creep law parameters issued from the references listed in bracket. C is the extra constant that allows varying the strength of phases II and III.

occurs in response to the delamination of the dense crustal root after 16 Myr. A detailed mechanical interpretation of the specific kinematics observed at crustal and upper mantle scale during these three stages follows.

4.1. Localization of crustal extension

At the beginning of the computation, the deformation is distributed in the upper crust ($\dot{\epsilon}^{\text{II}}$ in Fig. 5A), while the elastic core of the lithosphere, internally loaded by the embedded dense crustal root, deforms by downward flexure beneath the batholithic crust and upward flexure beneath the Basin and Range and Great Valley. The smaller rigidity of the decoupled crust of the Basin and Range results in a larger deflection of the Moho ($V_{y,\text{Moho}}$ in Fig. 5A) in the eastern side of the model. The disharmony between the wavelengths associated with Moho flexural deflection and the infinite wavelength implied by distributed strain in the upper crust causes lateral volume variations of the lower crustal viscous channel. They induce a 40 MPa over 80 km horizontal pressure gradient ($\Delta\sigma^{\text{I}}$ in 5A) associated with a westward couette flow (high strain rate $>10^{-14}$ s⁻¹, Fig. 5A), which length scale is thus being controlled by the wavelength of lithospheric flexure. Because of the finite size of the flow, a large horizontal velocity gradient exists at the top of the Basin and Range bulge and leads to the localization of strain in the elasto-plastic part of the crust after 6.3 Myr (compare $\dot{\epsilon}^{\text{II}}$ Fig. 5A and B).

During this phase of crustal-scale localization, the upper part of the mantle lithosphere is being stretched with a shallow level of necking [31] so that its upper part behaves as a continuous elastic plate (σ^{II} Fig. 5B) but its rigidity decrease with time. As in the preliminary models, the part of the lithosphere located below the 900 °C isotherm is convectively unstable. However, the chemical density contrast between the root and the regular

lithosphere infers a larger growth rate beneath the batholith. The warm symmetric return flows of this dominant cell are superimposed on the flexural effect and participate thermally to the weakening of the lithosphere.

4.2. Lithospheric break-off

From 6.3 to 11.6 Myr, the passive, i.e., boundary conditions driven, extension continues to be accommodated by lithospheric necking and a crustal listric normal shear zone [32] so that the edge of the batholith slowly subsides in the hanging wall of the normal faults. As necking increases, the mantle lithosphere rigidity decreases. The load due to the crustal root being constant, the vertical deflection never reaches an equilibrium allowing the couette flow to continue in the lower crust.

At 11 Myr, as the strength of the mantle lithosphere locally drops from 100 MPa to less than 10 MPa in the rift zone (compare σ^{II} in Fig. 5B and C), allowing the crustal and mantle shear zones to connect (compare $\dot{\epsilon}^{\text{II}}$ in Fig. 5B and C). The mantle lithosphere break-up is marked in the topography by the acceleration of the subsidence rate of the edge of the batholith (Fig. 5E). This new localized weakness allows the asthenosphere

Table 2
Model parameters and issue

Model	G.B. (II)	B.R. (III)	G.V.	M.B.	Delam.	Rel.time
A	$C=10^2$	$C=10^2$	I	V	Yes	12
B	$C=10^2$	$C=10^2$	VIII	V	Yes	12
C	$C=10^4$	$C=10^4$	I	V	Yes	9
D	$C=1$	$C=1$	I	V	No	N.A.
E	$C=10^4$	$C=10^4$	I	VII	No	N.A.

G.B.: granitic batholith, B.R.: Basin and Range; G.V.: Great Valley; M.B.: mafic batholith; Delam.: occurrence of delamination in the model; Rel.time: relative timing between the onset of normal faulting and the uplift of the crest.

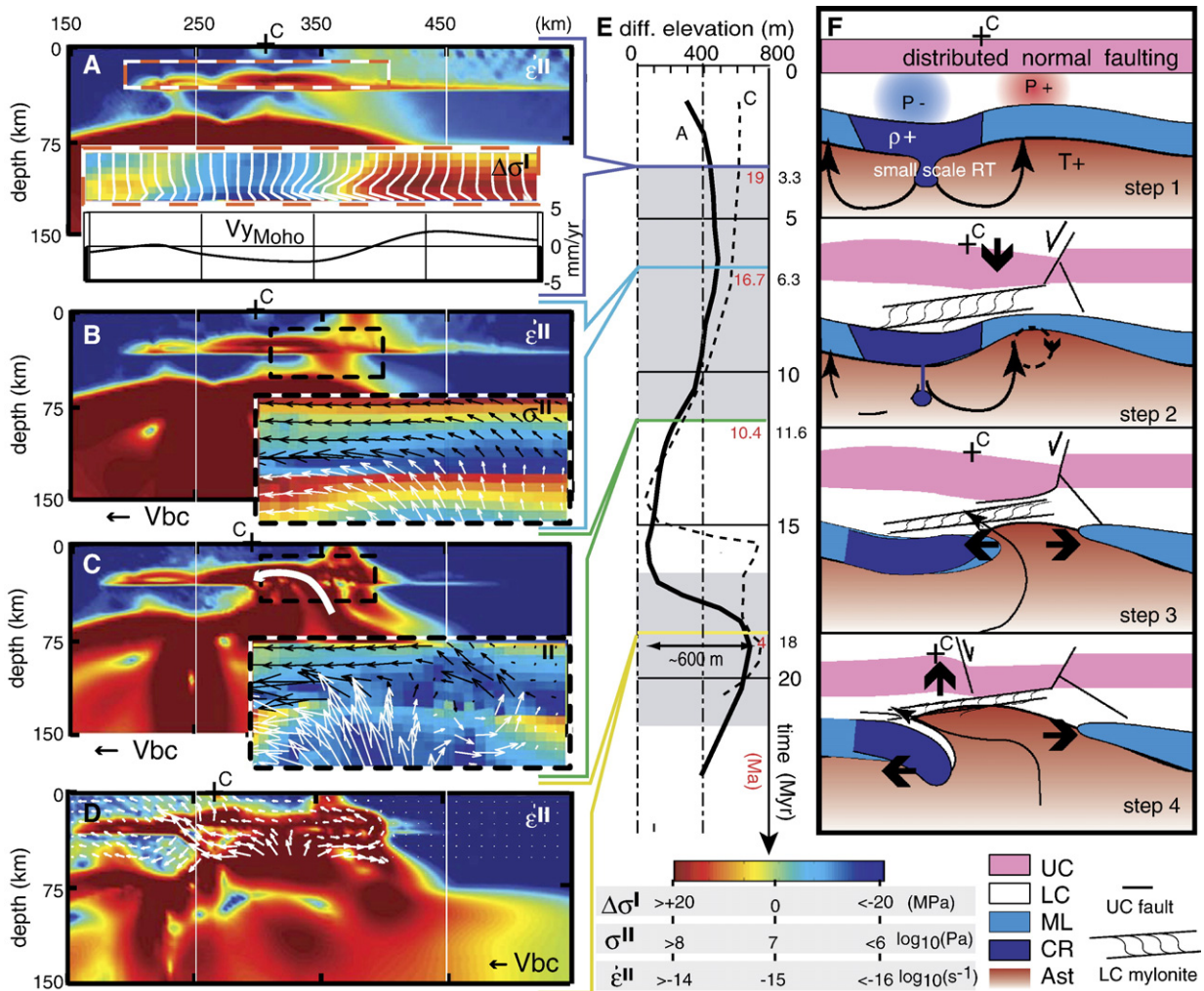


Fig. 5. A delamination model for the Southern Sierras. The plot (A–D) represented corresponds to Model A. The figure in (E) represents the evolution of the elevation of the crest of the Sierras (point C Fig. 4) with time; Thick line: Model A; Dashed line: Model C. Both models present the same overall kinematics (F) but the uplift phase happens earlier in the time (dashed line in E). Details description of the models: (A) the thin white lines denotes horizontal component of velocity along vertical profiles in the low viscosity channel. (A–D) The arrows represent velocity vector scaled to the velocity imposed at boundary condition (V_{bc}). $\dot{\epsilon}^{\text{II}}$, $\Delta\sigma^{\text{I}}$ and σ^{II} stand, respectively, for second invariant of strain rate (i.e., maximum shear strain rate), dynamic pressure and second invariant of stress (i.e., radius of Mohr circle); $V_{y_{\text{Moho}}}$ is the vertical velocity at the Moho. (F) UC, LC, ML, CR and Ast are respectively upper crust, lower crust, mantle lithosphere, crustal root and asthenosphere.

to rise within the thermally denser surrounding lithosphere ($\Delta\rho=33 \text{ kg m}^{-3}$, see Eq. (A3)). However, the asthenospheric flow is forced to spread at the base of the lower crust because of the chemical density contrast ($\Delta\rho=550 \text{ kg m}^{-3}$, Table 1). The velocity vectors pointing to the east in the rift zone imply that the total extension rate exceeds the boundary condition rate and hence that rifting becomes active.

4.3. Delamination

Because the crustal root is denser than the mantle lithosphere ($\Delta\rho=110 \text{ kg m}^{-3}$, Table 1), westward

spreading of the asthenosphere is favored and follows the same shear zone that previously accommodated the extension in Death Valley (Fig. 5D). This horizontal flow triggers the delamination of the crustal root from 16 to 20 Myr. From 18 Myr (Fig. 5D), the location of extension begins to migrate from the west-dipping fault of Death Valley to an east-dipping fault located at the edge of the batholith. The migration of upper crustal plate boundary is achieved at 22 Myr when the crustal root is removed and forms an anomalously high-density cold temperature elongated body dipping to the east below the western Sierras and Great Valley (see Fig. 8).

5. Sensitivity to input parameters

5.1. Initial thickness of the channel (Models A, C and D)

A reduction of the thickness of the low-viscosity channel reduces the diffusivity of the flow and increases the relative timing between the onset of the Death Valley

extension and lithospheric break-up. Model C ($C=10^4$) delaminates after 14 Myr while Model A ($C=10^2$) reaches the same state 3 Myr later (Fig. 5E compare the thin dashed curve and thick curve).

For thickness below 10 km (Model D), delamination does not occur in the models. During the first 10 Myr, the deformation localizes close to the edge of the batholith on two set of grabens (Fig. 6A) that

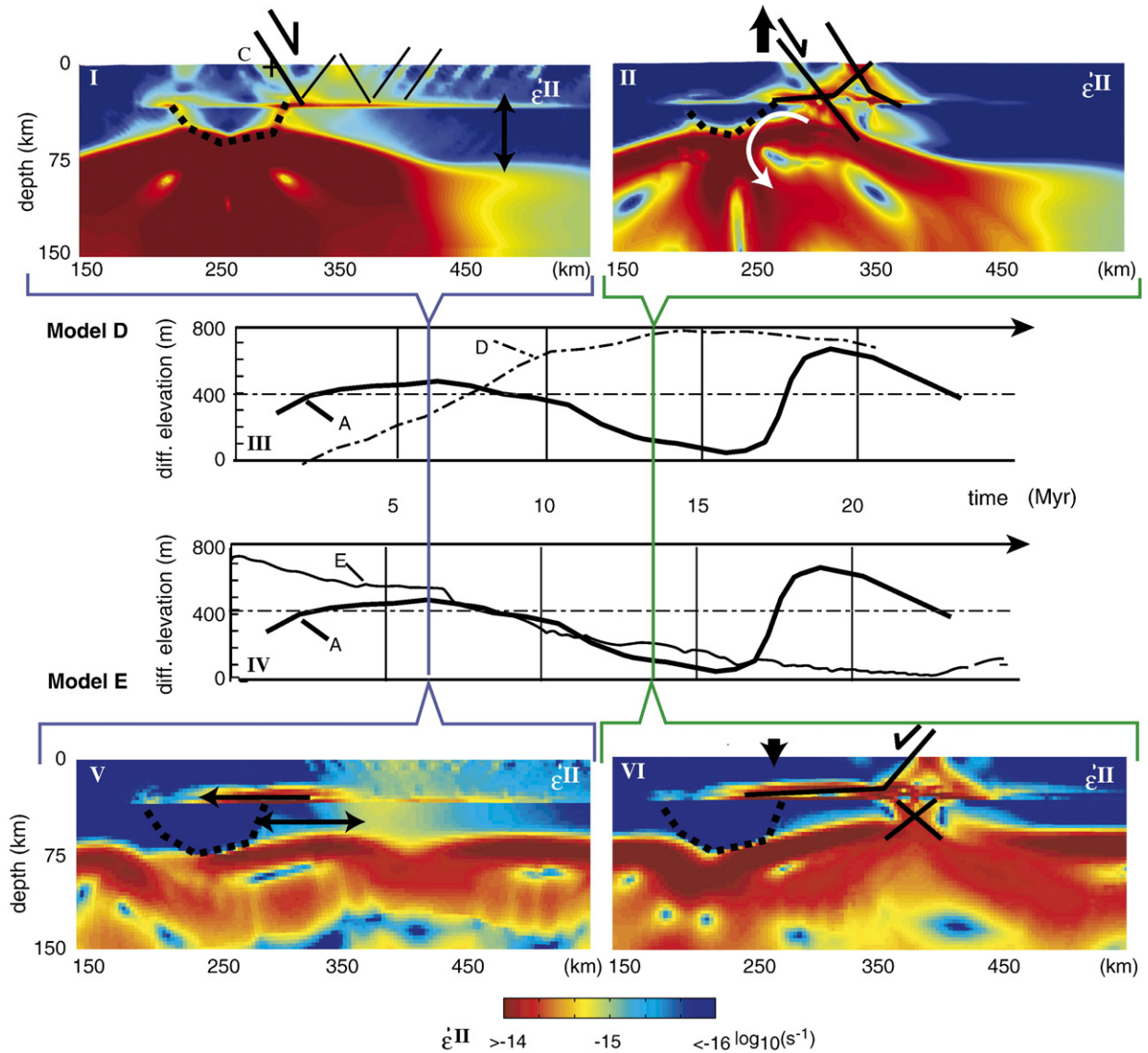


Fig. 6. Limiting factor to delamination. The color scale pictures are representing the second invariant of strain rate, the dashed lines are the contours of the mafic batholith crust in the models. Thick arrows indicate the position and displacement of the edge of the batholith. Top: Model D: Note the absence of lower crustal channel flow at the onset of the extension (I) and the continuous uplift of the crest along (III) time. Extension occurs on two set of grabens (I) that tends to localize on one with the time (II). Extension localizes closer to the root that gets convectively eroded by the side (white arrow, II). Bottom: Model E, the batholith subsides for 20 Myr (IV). Channel flow occurs in response to loading (V) but runs on a longer distance than in Fig. 5A. Once strain localizes in the crust, point C is located in the hanging wall of the low-angle normal fault but further away so that subsidence has a slower rate (IV). After 20 Myr, a rift has developed far from the batholith that remains completely stable (VI).

correspond to the two strong levels of the model: the upper crust and the upper mantle lithosphere. In response to lithospheric scale faulting, the edge of the batholith uplifts by flexure (Fig. 6C). The mantle lithosphere locally loses its flexural strength through convective erosion from its base. As the strain localizes right at the edge of the batholith, the eclogitic root is also slowly eroded. As a result, the strain localizes on the central horst and on an east-dipping normal fault at the edge of the Batholith (Fig. 6B). Uplift reaches its maximum at 15 Myr with the onset of low angle normal faulting (Fig. 6). From a kinematic point of view, this maximum corresponds to the 6.3 Myr maximum of Model A. However, after 13 Myr, half of the root has been eroded, and one may infer that no new acceleration of uplift will occur as its buoyancy source has essentially disappeared. In conclusion, very thin (less than 5 km) or non-existing lower crustal channel models favor the narrow rift mode [33] and, hence, allow for a greater amount of initial flexural uplift on a 15 Myr timescale, but they do not lead to the secondary fast uplift event observed in the southern Sierra [16] because delamination does not occur.

5.2. Influence of the initial geotherm

The high thermal gradient at the base of the root is a necessary condition for delamination to occur. It allows the formation of a convection cell localized below the batholith, enhances the necking of the lithosphere, and favors a rapid transition from passive to active rifting [34].

If the high temperature gradient of the initial geotherm is located deeper than the maximum depth of the root then the root is fully stable until its base warms either by small scale convective removal of the lithospheric base or conductive heating. We emphasize that other factors such as the removal of the oceanic slab or the rapid infilling of a slab window may have caused the warm upwelling that is needed to ensure the transition from active to passive rifting.

5.3. influence of the crustal root rheology

If the viscosity of the crustal root is sufficiently larger than the viscosity of the mantle to overcome the chemical density ratio effect, that is, if $\eta_r \geq ((\alpha_v \Delta T \rho_r + \rho_r - \rho_m) / \alpha_v \Delta T \rho_m) \eta_r$, then the convective cell located below the root may also be inhibited. Using $\Delta T = 300$ K, $\rho_m = 3300$ kg m⁻³ and $\alpha_v = 3 \times 10^{-5}$ K⁻¹, this ratio

ranges between 2.7 and 7.8 for a root density ρ_r ranging from 3350 to 3500 kg m⁻³.

Model E corresponds to the hypothesis of a high viscosity root. Because the localization of extension in the crust is controlled by flexure under the loading of the root, as in model A, crustal localization occurs at the top of the flexural bulge. Since the convective cell located below the batholith grows at smaller rate than elsewhere at the base of the lithosphere, the flexural deflection due to internal loading has a longer wavelength than in Model A. Hence, strain localizes further away from the batholithic root (compare Fig. 6E and 5B). The elevation of the edge of the batholith with time (thin curve compared to Model A thick curve Fig. 6D) only indicates a slow subsidence of the edge of the batholith, located too far from the rifting the batholith constitutes a strong elastic core within the lithosphere (Fig. 6F).

5.4. Strength of the Great Valley

Models A and B are two end members with different strengths of the Great Valley crust; Model A with a relatively stiff quartzite and Model B with a very stiff dry diabase (see Table 1 for parameters). Because the stiff Great Valley model (Model B), unlike all the other models presented here, did not have an initial topography in isostatic equilibrium, the inception of extension was almost instantaneous and induces a 4 Myr shift between the two curves (Fig. 7A). Nevertheless, from the inception of upper crustal strain localization within the Basin and Range, the topographic evolution of both models shows similar trends and time lapse indicating that the viscosity of the Great Valley lower crust does not affect the timing between the inception of the new plate and delamination. However, if this rheological parameter does not affect the timing and kinematics of the formation of the Death Valley relatively to fast uplift of the Sierra Nevada, it clearly affects the amplitude elevation change of the crest of the Sierra. Indeed, the crest of Model B is marked by an extra phase of subsidence of 1.5 km that lasts for 2–3 Myr and at the removal, its uplift is much larger as it accounts for both the elastic rebound due to the removal of the dense batholithic root and flexural uplift due to the load exerted by the root on the Great Valley. As the drip is strongly coupled to the Great Valley lithosphere, delamination leads to the formation of a 4 km deflection in the Great Valley associated with a bulge of 150 km half wave length

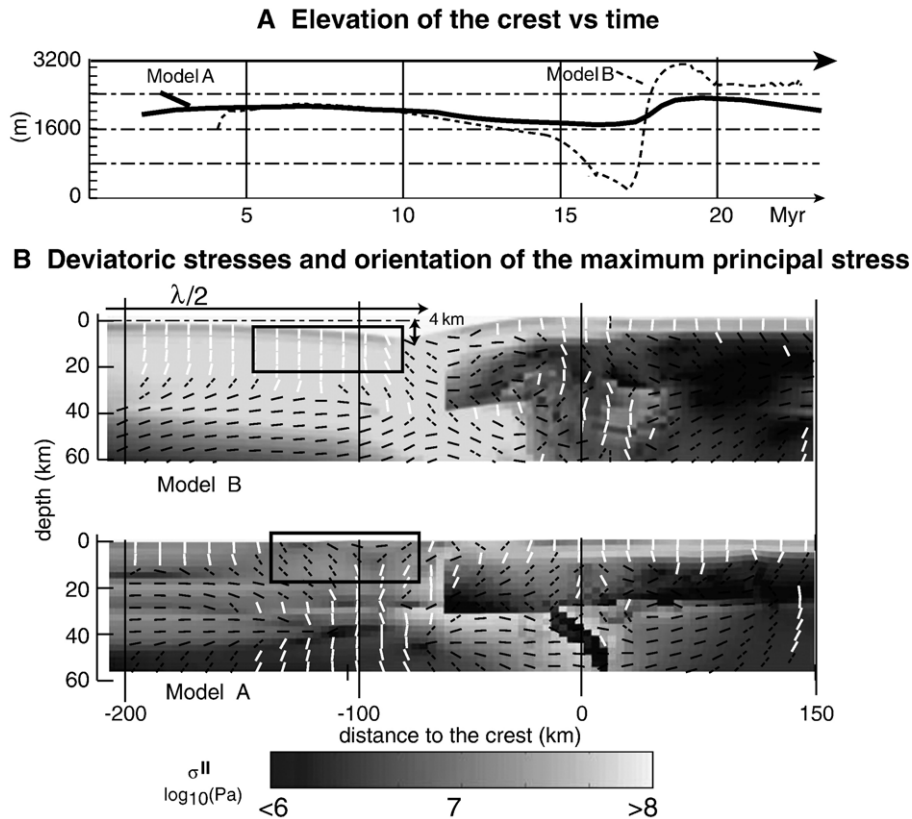


Fig. 7. Influence of the strength of the Great Valley crust. (A) Elevation of the crest of the batholith through time for Model A and B. (B) The gray scale background represents the second invariant of stress also called tectonic stress. The dashes are oriented in the direction of the maximum principal stress σ_I . Each style of dash corresponds to range of orientations with geodynamic relevance: vertical to 65° (white, extension), horizontal to 25° (black continuous, compression), intermediate (black double dashed; important component of simple shear).

(λ) that is clearly visible in the post-delamination state of stress (Fig. 7B).

6. Model validation

The 10 km limiting initial thickness for the low-viscosity channel is not inconsistent with the overall history of the region which has a number of metamorphic core complexes that have been associated mechanically with thick low-viscosity channels [33]. All the models in which instability occurred generally fit the present-day gravity and seismic structures. Moreover, the rapid uplift is preceded by a subsidence phase that always last for about 2 Myr (e.g., Fig. 7). In terms of the spacing and timing of the major tectonic events which have affected the region since the middle Miocene (the initiation of extension in the Death Valley region at 16 Ma, the inception of the Sierra Nevada micro-plate at 10 Ma, and the recent uplift of the Sierra Nevada at 5 to 3–2 Ma) are only reproduced in Models A and B.

The net increase of elevation (Fig. 7 solid line) of the Model A is comparable (600 m) to the inferred uplift [16] while Model B predicts 3000 m. The main topographic features such as the asymmetry of the Sierras and several depressions to the east are resolved with reasonably good spacing. The evolution of the topography of the eastern Sierra and especially the subsidence phase that precede the uplift is consistent with the sedimentation history of Owens Lake, especially with the thick sections of Upper Miocene–Lower Pliocene lake sediments that are now uplifted and tilted on its eastern flank [35]. None of the models A or B produces a good fit to the subsidence data of the Great Valley (Model A produce almost no subsidence and Model B produce a 4 km hole while only 1 km of sedimentation occurs during the last 2–3 Myr with two phases of acceleration (Z. Foster, personal communication). The actual strength of the Great Valley probably lies between those two end members. This parameter could be constraint by varying the strength

of the transition between the accretionary complex in the western Great Valley subsurface and the Mesozoic arc basement to the east and comparing the results with the subsidence data on the Tulare sub-basin. This is behind the scope of this study which focuses on the relation between the extension in the Death Valley and the recent uplift of the Sierra. Nevertheless, the post-delamination state of stress (Fig. 7B) leads to the rejection of Model B because this model predicts extensional regime at the location of the Coast Range fold while Model A predicts compression due to extra-topographic load of the Sierra.

To further validate Model A at larger scale, the Bouguer gravity anomaly and direct model of the body waves slowness were computed using the same modal mineralogical compositions, database and algorithm as [17] to obtain density and P-waves velocities as a function of pressure and temperature.

Gravity anomalies allow comparison of the distribution of the masses inside the crust and Moho deflections. Because acceleration of gravity is the gradient of the gravity potential Φ created by the distribution of the masses in the model, synthetic anomalies can be computed using the same FEM code as for the initial geotherm (see Appendix B). The position of the reference Geoid has been set to the height of the left end side of the domain. Density anomalies ($\Delta\rho$) have been computed using a reference density model that assumes a contrast of 500 kg m^{-3} at the Moho. The Bouguer anomaly of Model A (Fig. 8A) has a comparable amplitude and width as observed [30].

At upper mantle scales, the direct models of the body waves slowness anomalies have been plotted with the same color scale as the seismic tomographic model [17] and shows good agreement with its -1% and $+1\%$ contours (Fig. 8B). Hence, the geometry of the observed drip and synthetic drip are similar and located below the Great Valley. Nevertheless, in our direct model, the chemical density contrast caused by anomalously dense crustal root does not completely overcome the temperature gradient. Hence, the high-density eclogitic root is located in the high-velocity anomaly (-1% slowness) beneath the Great Valley as in gravity inferred density model [30], and not below the Sierra as inferred by seismic tomography [17]. Varying the modal composition of the root, we found that the results are highly sensible to the garnet content of the ultra-mafic crustal root. Assuming $50\% \text{Grt}-50\% \text{Cpx}$ (M. Ducea, personal communication) instead of the $(30\% \text{Grt}-70\% \text{Cpx})$ proposed by [17], the ultra-mafic root becomes transparent. Moreover, the return flows of the instability put in contact the cold remnant of the garnet peridotites

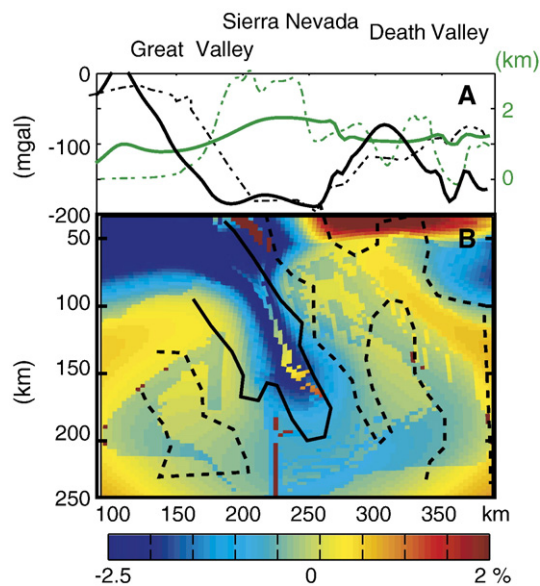


Fig. 8. Geophysical validation of the model. (A) Modeled (solid lines) and observed (dashed line [25]) Bouguer gravity anomaly (black lines) and topography (green lines) at the level of the southern profile (Fig. 1). (B) Direct P-wave slowness anomaly model compared to $+1\%$ (solid line) and -1% (dashed lines) iso-contours of the tomographic inversion [17].

continental lithosphere and the warm harzburgites of the mantle upwelling and is mainly responsible for the east-dipping fabric of the direct model.

7. Geodynamical implications of the results

Even though we favored the hypothesis that the recent uplift of the Sierra Nevada was driven by gravitational instability, the elasto-plastic weakening effect on the strength of the lithosphere as well as structural effect related to the crust/mantle decoupling were not neglected in our modeling. In our models, root removal occurs when the lithosphere behaves as a ‘jelly sandwich’ in which the lower/middle crust must be sufficiently weak for pressure gradients to accelerate the thinning of the lithosphere around the dense crustal root. In that case, the dense root sinks as a rigid finite body in a viscous fluid. Hence, by analogy to a Stoke’s problem, once the instability has occurred, i.e., once the lithosphere has lost its strength, its characteristic timescale is intrinsically shorter than in the RT instability [5,17,18] because its sinking rate is controlled by the viscosity of the asthenosphere (10^{19} Pa s in the models) rather than by the viscosity of the lithosphere (10^{21-25} Pa s in the models). An important prediction is that the local loss of strength of the lithosphere is a long process ($\sim 15-30 \text{ my}$ if we include the time needed to warm up the base of the eclogitic root)

while the time scale of its removal is short 1–2 Myr. In our model, the high degree of non linearity is achieved through geometrical softening mechanism that are well known in engineering. This non-linearity cannot be explained with any of the laboratory-inferred rheologic parameters [2, 18] nor with intrinsic visco-elastic effects [20, 36]. As the lithosphere act as a boundary conditions to flow in the mantle, the coupling of the crust to the mantle is shown to be an important parameter in geodynamics, perhaps significant at global scale.

Our model is not only preferred to RT models because it predicts the timing and location of the drip but also because it predicts a realistic evolution of the elevation of the Sierra Nevada through time, the timing of Sierran microplate inception, and the geometry of major extensional structures of the region coherently with a mechanical model. Delamination may not be restricted to the southern Sierra but could also apply to other Cordilleran-type arcs where root removal is believed to have occurred. Testable predictions of the delamination models are that drips produce sharp (few kilometers) seismic velocity contrasts in the upper mantle and that uplift is preceded by ductile shear zones that dip towards the drip. According to this model, the timing of the removal does not constrain the viscous strength of the lithosphere as in the RT models [18]. However, the timing between the onset of normal faulting and delamination constrains the diffusivity of the flow in the lower crust.

Acknowledgements

This represents contribution number 9156 of the Division of Geological and Planetary Sciences and 35 of the Tectonics Observatory. Partially supported by the NSF under EAR-0205653 and the Gordon and Betty Moore Foundation. We thank Zorka Foster for help with the structural map and fruitful discussion. We thank Muriel Gerbault, an anonymous reviewer, and Scott King for helping to improve the manuscript and A. Poliakov and Y. Podladchikov, the main contributors to Paravoz, for access to their code.

Appendix A

The numerical code, Paravoz [20], used here is a well tested 2D thermo-mechanical code based on the FLAC method (Fast Lagrangian Analysis of Continua). The software solves Cauchy equation of motion for a continuum in term of stress and displacement (A1) and heat transfer (A2) using a fully coupled (including thermal stress/shear heating) explicit scheme on a Lagrangian

mesh using a mixed (element/nodes) discretization to avoid mesh locking [19].

$$\rho g_i + \frac{\partial \sigma_{ij}}{\partial x_j} = \rho \frac{\partial V_i}{\partial t} \quad (\text{A1})$$

$$\frac{DT}{Dt} = \frac{\partial}{\partial x_i} \chi \frac{\partial T}{\partial x_i} + \frac{H_r}{\rho C_p} \quad (\text{A2})$$

ρ , g , σ , x , V , t , χ , T , H_r and C_p mean density, gravity acceleration, stress tensor, spatial coordinates, velocity, time, thermal diffusivity, temperature, radiogenic heat production and heat capacity. Einstein summation applies for repeated indices. Heat advection is implicitly solved considering the rate of deformation of the mesh as indicated by the total time derivative D in (A2). Density depends on temperature following the Boussinesq approximation and on the chemical composition of the rocks (A3) where ρ_χ , α_ν are, respectively, the chemical reference density and the adiabatic coefficient of thermal expansion.

$$\begin{cases} \rho = \rho_\chi + \Delta\rho_T \\ \Delta\rho_T = \rho_\chi \alpha_\nu \Delta T \end{cases} \quad (\text{A3})$$

Large strain computations are allowed by remeshing as soon as one of the corners of the triangular mesh reaches a critical minimum angle of 8°. The remeshing process includes linear interpolation of nodal values (velocity, temperature) and closest neighbour redistribution of elementary values (stresses, physical properties including finite strain).

Maxwell visco-elastic (A4) or Mohr–Coulomb elasto-plastic (A6) (A7) (A8) constitutive laws are used alternately to relate stress to the strain and its derivative following a pseudo-thermodynamic rule, i.e., by choosing which one of the both rheology produces the lowest value for the second invariant of stress tensor. Maxwell rheology is implemented as follows:

$$\begin{cases} \sigma_{ij} = \tau_{ij} + \delta_{ij} \bar{\sigma}; e_{ij} = \dot{\epsilon}_{ij} - \delta_{ij} \dot{\bar{\epsilon}} \\ \dot{\tau}_{ij} = 2G \left(e_{ij} - \frac{\tau_{ij}}{2\eta_{\text{shear}}(T, e^{\text{II}})} \right) \\ \bar{\sigma} = K \epsilon_{ii} \end{cases} \quad (\text{A4})$$

η_{shear} is the effective dynamic viscosity [37]. It varies from 10^{19} to 10^{25} Pa s depending on n , Q (J) and A (Pa^{-n}).

$$\eta_{\text{shear}}(T, e^{\text{II}}) = 1/4 e^{\text{II}(\frac{1}{n}-1)} (3A/4)^{\frac{-1}{n}} \exp\left(\frac{Q}{nRT}\right) \quad (\text{A5})$$

δ_{ij} is the Kronecker delta, G and K are the shear and bulk modulus, respectively, and e^{II} is the second

invariant of the strain rate tensor $\dot{\epsilon}_{ij}$. Einstein summation of the indices apply.

Mohr–Coulomb elasto-plastic non associated flow rule [38] is taken into account if the state of stress reaches the yield criteria f^s , which depends on the internal friction angle Φ of the material and on the amplitude of the minor and major principal stress σ_3 and σ_1 , respectively.

$$N_\Phi = \frac{1 + \sin\Phi}{1 - \sin\Phi}$$

$$f^s = \sigma_1 - N_\Phi \sigma_3 + 2Co\sqrt{N_\Phi}$$

$$f^s = 0 \Leftrightarrow \text{yielding} \quad (\text{A6})$$

If the yield criterion is reached, plastic strain ϵ^{plas} is derived from the plastic potential Q^s , which depends on the dilatancy angle Ψ .

$$N_\Psi = \frac{1 + \sin\Psi}{1 - \sin\Psi}$$

$$Q^s = \sigma_1 - N_\Psi \sigma_3$$

$$\dot{\epsilon}^{\text{plas}} = \lambda \frac{\partial Q^s}{\partial \sigma}; \quad \dot{\epsilon}^{\text{plas}} + \dot{\epsilon}^{\text{elas}} = \dot{\epsilon} \quad (\text{A7})$$

The plastic multiplier λ is found assuming that the stresses keep staying on the yielding surface (i.e., $\dot{f}^s=0$) for consistency reasons. One may note that assuming non associated flow rule, elastic stress rate are non null and actually allows for the localization of shear bands.

Appendix B. FEM Laplace Solver

The FEM-based code (Finite Element Method) used to compute gravity anomaly and initial geotherm is written in MATLAB© language and solves

$$C_1 \left(\frac{\partial^2 U}{\partial x^2} + \frac{\partial^2 U}{\partial z^2} \right) = -C_2 P(x, z) + \frac{\partial U}{\partial t} \quad (\text{B1})$$

Unknown U is thus discretized in space using bilinear shape functions in the isoparametric element following $U(\eta, \xi) = \sum_{j=1}^{\text{ns_shape}} U_j H_j(\eta, \xi)$ and discretized explicitly in time as

$$\frac{\partial U}{\partial t} = \frac{U - U^{\text{old}}}{\Delta t} \quad (\text{B2})$$

Replacing U by its discrete form \hat{U}_j at local node j , integrating by parts, discretizing the integration with mapping from element (i, j) to global (I) numbering and assuming conservation of energy (incoming flux = outgoing flux between the elements or null flux on the

boundary), the system (R) of N (global number of degree of freedom) discrete equations (R_i) becomes

$$R_i = 0 = \sum_{\text{ELTS}} \sum_{ip} w_{ip} \det \mathbf{J}_{ip} \left(\left[-C_1 \left(\frac{\partial H_i}{\partial \eta} \frac{\partial H_j}{\partial \eta} + \frac{\partial H_i}{\partial \xi} \frac{\partial H_j}{\partial \xi} \right) + H_i H_j \right] \Big|_{xip} \hat{U}_{j\text{loc}} - H_i H_j \Big|_{xip} \left(C_2 \hat{P}_j + \hat{U}_j^{\text{old}} \right) \right) \quad (\text{B3})$$

After imposing the boundary conditions, we use the linear solver for sparse system of equations, taken directly from MATLAB© ('sparse' and '\') functions) to solve R for \hat{U}_j .

Variables and constants should be set as follows.

For the steady-state heat problem: $U(x, z) = T(x, z)$, the temperature, $C_1 = k$, the thermal conductivity, $C_2 = \rho$, the density and $P = e^{\frac{-z}{z_{\text{ref}}}} \Pi$ where Π is the radiogenic heat production by unit masse;

For the transient heat problem: $U(x, z) = T(x, z)$, the temperature, $C_1 = dt\kappa$, where κ is the thermal diffusivity, $C_2 = dt/c$, where c is the thermal capacity and $P = e^{\frac{-z}{z_{\text{ref}}}} \Pi$;

For the gravity field problem: $U(x, z) = \Delta \Phi(x, z)$, the anomalous gravity potential, $C_1 = 1$, $C_2 = 2\pi G$, where G is the gravitational constant (note that this form is valid inside the Earth) and $P = \Delta \rho(x, z) = \rho(x, z, P, T) - \rho_{\text{ref}}(x, z)$. The amplitude of the gravity anomaly $\Delta g = \frac{\partial \Delta \Phi}{\partial z} \Big|_{z=z_{\text{ref}}}$ is computed after having flattened the topography to the reference altitude z_{ref} such that $\frac{\partial \Delta \Phi}{\partial x} \Big|_{z=z_{\text{ref}}} \equiv 0$. The reference Geoid z_{ref} is arbitrarily chosen to be the top left corner of the model.

The code has been benchmarked for its thermal part with semi-analytical solutions [39].

References

- [1] P. Molnar, G.A. Houseman, The effects of buoyant crust on the gravitational instability of thickened mantle lithosphere at zones of intracontinental convergence, *Geophys. J. Int.* 158 (2004) 1134–1150.
- [2] C.P. Conrad, P. Molnar, The growth of Rayleigh–Taylor-type instabilities in the lithosphere for various rheological and density structures, *Geophys. J. Int.* 129 (1) (1997) 95–112.
- [3] P. Molnar, G.A. Houseman, C.P. Conrad, Rayleigh–Taylor instability and convective thinning of mechanically thickened lithosphere: effects of non-linear viscosity decreasing exponentially with depth and of horizontal shortening of the layer, *Geophys. J. Int.* 133 (3) (1998) 568–584.
- [4] G. Zandt, H. Gilbert, T.J. Owens, M. Ducea, J. Saleeby, C.H. Jones, Active foundering of a continental arc root beneath the southern Sierra Nevada in California, *Nature* 431 (7004) (2004) 41–46.

- [5] J. Saleeby, M. Ducea, D. Clemens-Knott, Production and loss of high-density batholithic root, southern Sierra Nevada, California, *Tectonics* 22 (6) (2003).
- [6] M. Ducea, J. Saleeby, A case for delamination of the deep batholithic crust beneath the Sierra Nevada, California, *Int. Geol. Rev.* 40 (1) (1998) 78–93.
- [7] C.H. Jones, H. Kanamori, S.W. Roecker, Missing roots and mantle drips—regional $P(N)$ and teleseismic arrival times in the southern Sierra-Nevada and vicinity, California, *J. Geophys. Res.-Solid Earth* 99 (B3) (1994) 4567–4601.
- [8] D.F. Argus, R.G. Gordon, Current Sierra-Nevada North-America motion from very long base-line interferometry—implications for the kinematics of the western United States, *Geology* 19 (11) (1991) 1085–1088.
- [9] C.D. Henry, M.E. Perkins, Sierra Nevada-Basin and Range transition near Reno, Nevada: two-stage development at 12 and 3 Ma, *Geology* 29 (2001) 719–722.
- [10] B.E. Surpless, D.F. Stockli, T.A. Dumitru, E.L. Miller, Two-phase westward encroachment of Basin and Range extension into the northern Sierra Nevada, *Tectonics* 21 (1) (2002).
- [11] F.C. Monastero, A.E. Sabin, J.D. Walker, Evidence for post-early Miocene initiation of movement on the Garlock fault from offset of the Cudahy Camp Formation, east-central California, *Geology* 25 (3) (1997) 247–250.
- [12] D.P. Loomis, D.W. Burbank, The stratigraphic evolution of the El Paso Basin, southern California; implications for the Miocene development of the Garlock Fault and uplift of the Sierra Nevada, *Geol. Soc. Amer. Bull.* 100 (1) (1988) 12–28.
- [13] J.R. Unruh, The uplift of the Sierra Nevada and implications for Late Cenozoic epeirogeny in the western Cordillera, *Geol. Soc. Amer. Bull.* 103 (1991) 1395–1404.
- [14] B. Wernicke, G.J. Axen, J.K. Snow, Basin and Range extensional tectonics at the latitude of Las Vegas, Nevada, *Geol. Soc. Amer. Bull.* 100 (1988) 1738–1757.
- [15] J. Saleeby, Z. Foster, Topographic response to mantle lithosphere removal in the southern Sierra Nevada region, California, *Geology* 32 (3) (2003) 245–248.
- [16] M.K. Clark, G. Maheo, J. Saleeby, K.A. Farley, The non-equilibrium landscape of the southern Sierra Nevada, California, *GSA Today* 15 (9) (2005) 4–10.
- [17] O.S. Boyd, C.H. Jones, A.F. Sheehan, Foundering lithosphere imaged beneath the Southern Sierra Nevada, California, USA, *Science* 305 (5684) (2004) 660–662.
- [18] P. Molnar, C.H. Jones, A test of laboratory based rheological parameters of olivine from an analysis of late Cenozoic convective removal of mantle lithosphere beneath the Sierra Nevada, California, USA, *Geophys. J. Int.* 156 (3) (2004) 555–564.
- [19] P.A. Cundall, M. Board, A microcomputer program for modeling large-strain plasticity problems, in: B.A. A (Ed.), *Numerical Methods in Geomechanics*, Innsbruck, 1988, pp. 2101–2108.
- [20] A. Poliakov, P.A. Cundall, Y.Y. Podladchikov, V. Lyakhovskiy, An explicit inertial method for the simulation of visco-elastic flow: an evaluation of elastic effect in two and three layers models, in: D.B. Stone, S.K. Runcorn (Eds.), *Flow and Creep in the Solar System: Observation, Modelling and Theory*, Kluwer academic publishers, Netherlands, 1993, pp. 175–195.
- [21] T. Atwater, Implications of plate tectonics for the Cenozoic tectonic evolution of western North America, *Geol. Soc. Amer. Bull.* 81 (1970) 3513–3536.
- [22] T. Atwater, J.M. Stock, Pacific–North America plate tectonics of the Neogene southwestern United States: an update, *Int. Geol. Rev.* 40 (5) (1998) 375–402.
- [23] B. Parsons, J.G. Sclater, An analysis of the variation of ocean floor bathymetry and heat flow with age, *J. Geophys. Res.-Solid Earth* 82 (1977) 803–827.
- [24] E.B. Burov, M. Diament, The effective elastic thickness (T-E) of continental lithosphere—what does it really mean, *J. Geophys. Res.-Solid Earth* 100 (B3) (1995) 3905–3927.
- [25] M. Ducea, J. Saleeby, Crustal recycling beneath continental arcs: silica-rich glass inclusions in ultramafic xenoliths from the Sierra Nevada, California, *Earth Planet. Sci. Lett.* 156 (1–2) (1998) 101–116.
- [26] G.C. Gleason, J. Tullis, A flow law for dislocation creep of quartz aggregates determined with the molten-salt cell, *Tectonophysics* 247 (1–4) (1995) 1–23.
- [27] L. Le Pourhiet, E. Burov, I. Moretti, Rifting through a stack of inhomogeneous thrusts (the dipping pie concept), *Tectonics* 23 (4) (2004) TC4005.
- [28] B. Evans, C. Goetze, Temperature-variation of hardness of olivine and its implication for polycrystalline yield stress, *J. Geophys. Res.-Solid Earth* 84 (NB10) (1979) 5505–5524.
- [29] B. Wernicke, R. Clayton, M. Ducea, C.H. Jones, S. Park, S. Ruppert, J. Saleeby, J.K. Snow, L. Squires, M. Flidner, G. Jiracek, R. Keller, S. Klemperer, J. Luetgert, P. Malin, K. Miller, W. Mooney, H. Oliver, R. Phinney, Origin of high mountains in the continents: the southern Sierra Nevada, *Science* 271 (5246) (1996) 190–193.
- [30] S. Ruppert, M.M. Flidner, G. Zandt, Thin crust and active upper mantle beneath the Southern Sierra Nevada in the western United States, *Tectonophysics* 286 (1–4) (1998) 237–252.
- [31] H. Kooi, S. Cloetingh, Lithospheric necking and regional isostasy at extensional basins. II—Stress-induced vertical motions and relative sea level changes, *J. Geophys. Res.-Solid Earth* 97 (12) (1992) 17,573–17,591.
- [32] N.J. Kuszniir, P.A. Ziegler, The mechanics of continental extension and sedimentary basin formation: a simple-shear/pure-shear flexural cantilever model, *Tectonophysics* 215 (1992) 117–131.
- [33] W.R. Buck, Modes of continental lithospheric extension, *J. Geophys. Res.-Solid Earth* 96 (B12) (1991) 20161–20178.
- [34] R.S. Huismans, Y.Y. Podladchikov, S.A.P.L. Cloetingh, Transition from passive to active rifting: relative importance of asthenospheric doming and passive extension of the lithosphere, *J. Geophys. Res.-Solid Earth* 106 (2001) 11,271–11,292.
- [35] S.B. Bachman, Pliocene–Pleistocene break-up of the Sierra Nevada–White-Inyo Mountains block and the formation of Owens Valley, *Geology* 6 (1978) 461–463.
- [36] B. Kaus, T. Becker, Effects of elasticity on the Rayleigh–Taylor instability: implications for large-scale geodynamics., *Geophys. J. Int.*, in press.
- [37] Y. Chen, J. Morgan, A non-linear rheology model for mid-ocean ridge axis topography, *J. Geophys. Res.-Solid Earth* 95 (1990) 17583–17604.
- [38] P.A. Vermer, The orientation of shear bands in biaxial tests, *Geotechniques* 40 (2) (1990) 223–236.
- [39] L. Le Pourhiet, *Modélisation thermo-mécanique de l’extension continentale: développements théoriques et applications au golfe de Corinthe (Grèce)*, PhD, UPMC Paris VI, 2004.
- [40] M.C. Tsenn, N.L. Carter, Upper limits of power law creep of rocks, *Tectonophysics* 136 (1–2) (1987) 1–26.
- [41] G. Hirth, D.L. Kohlstedt, Water in the oceanic upper mantle: implications for rheology, melt extraction and the evolution of the lithosphere, *Earth Planet. Sci. Lett.* 144 (1–2) (1996) 93–108.

- [42] W.F. Brace, D.L. Kohlstedt, Limits on lithospheric stress imposed by laboratory experiments, *J. Geophys. Res.-Solid Earth* 85 (NB11) (1980) 6248–6252.
- [43] Z.M. Jin, J. Zhang, H.W. Green, S. Jin, Eclogite rheology: implications for subducted lithosphere, *Geology* 29 (8) (2001) 667–670.
- [44] S.J. Mackwell, M.E. Zimmerman, D.L. Kohlstedt, High-temperature deformation of dry diabase with application to tectonics on Venus, *J. Geophys. Res.-Solid Earth* 103 (B1) (1998) 975–984.